

Turbulence in Continental Stratocumulus, Part II: Eddy Dissipation Rates and Large-Eddy Coherent Structures

Ming Fang · Bruce A. Albrecht · Virendra P. Ghate ·
Pavlos Kollias

Received: 3 December 2012 / Accepted: 15 October 2013 / Published online: 10 November 2013
© Springer Science+Business Media Dordrecht 2013

Abstract This study first illustrates the utility of using the Doppler spectrum width from millimetre wavelength radar to calculate the energy dissipation rate and then to use the energy dissipation rate to study turbulence structure in a continental stratocumulus cloud. It is shown that the turbulence kinetic energy dissipation rate calculated from the radar-measured Doppler spectrum width agrees well with that calculated from the Doppler velocity power spectrum. During the 16-h stratocumulus cloud event, the small-scale turbulence contributes 40 % of the total velocity variance at cloud base, 50 % at normalized cloud depth=0.8 and 70 % at cloud top, which suggests that small-scale turbulence plays a critical role near the cloud top where the entrainment and cloud-top radiative cooling act. The 16-h mean vertical integral length scale decreases from about 160 m at cloud base to 60 m at cloud top, and this signifies that the larger scale turbulence dominates around cloud base whereas the small-scale turbulence dominates around cloud top. The energy dissipation rate, total variance and squared spectrum width exhibit diurnal variations, but unlike marine stratocumulus they are high during the day and lowest around sunset at all levels; energy dissipation rates increase at night with the intensification of the cloud-top cooling. In the normalized coordinate system, the averaged coherent structure of updrafts is characterized by low energy dissipation rates in the updraft core and higher energy dissipation rates surround the updraft core at the top and along the edges. In contrast, the energy dissipation rate is higher inside the downdraft core indicating that the downdraft core is more turbulent. The turbulence around the updraft is weaker at night and stronger during the day; the opposite is true around the downdraft. This behaviour

M. Fang (✉) · B. A. Albrecht
Rosenstiel School of Marine and Atmospheric Science,
The University of Miami, 4600 Rickenbacker Causeway, Miami, FL 33149, USA
e-mail: mfang3219@hotmail.com; mfang@rsmas.miami.edu

V. P. Ghate
Division of Environmental Sciences, Argonne National Laboratory,
9700 S. Cass Ave, Argonne, IL, USA

P. Kollias
Department of Atmospheric and Oceanic Sciences, McGill University,
Montreal, QC, Canada

indicates that the turbulence in the downdraft has a diurnal cycle similar to that observed in marine stratocumulus whereas the turbulence diurnal cycle in the updraft is reversed. For both updraft and downdraft, the maximum energy dissipation rate occurs at a cloud depth = 0.8 where the maximum reflectivity and air acceleration or deceleration are observed. Resolved turbulence dominates near cloud base whereas unresolved turbulence dominates near cloud top. Similar to the unresolved turbulence, the resolved turbulence described by the radial velocity variance is higher in the downdraft than in the updraft. The impact of the surface heating on the resolved turbulence in the updraft decreases with height and diminishes around the cloud top. In both updrafts and downdrafts, the resolved turbulence increases with height and reaches a maximum at cloud depth = 0.4 and then decreases to the cloud top; the resolved turbulence near cloud top, just as the unresolved turbulence, is mostly due to the cloud-top radiative cooling.

Keywords Coherent structures · Continental stratocumulus · Energy dissipation rate · Radar observed spectrum width

1 Introduction

This is Part II of a two-part case study of the turbulence structure in continental stratocumulus clouds. Part I (Fang et al. 2014; hereafter F14) documents the temporal evolution of the large-scale forcing and the turbulence structures. In Part II, observations from the Atmospheric Radiation Measurement program Southern Great Plains site millimetre wavelength cloud radar are used to examine the turbulence coherent structures associated with 16 h of stratocumulus clouds at the top of the boundary layer observed over Lamont, Oklahoma from 0900 CST of 25 March 2005 to 0100 CST of 26 March 2005. The central focus here is the calculation of the eddy/energy dissipation rate ε from the millimetre wavelength cloud radar observed Doppler spectrum width.

The quantity ε can be calculated by using the variance of the radar measured radial velocities such as that used by Bouniol et al. (2003), Lothon et al. (2005), O'Connor et al. (2010), and Shupe et al. (2012). Because of the radar beam filtering effect, the radial velocity variance is primarily contributed by the resolved turbulence with scales larger than the radar beam size (Rogers and Tripp 1964; Srivastava and Atlas 1974). In this study, we calculate ε from the spectrum width, which is the square root of the second central moment of the Doppler spectrum and primarily relates to the subscale or unresolved turbulence with scales comparable or smaller than the radar beam size.

The potential of using the Doppler spectrum width to obtain ε has been noted for decades (Rogers and Tripp 1964; Brewster and Zrnić 1986; Istok and Doviak 1986; Kollias et al. 2001), but Gossard et al. (1998) pointed out that many attempts to use the spectrum width from vertically pointed radars to estimate turbulence have not met with success because the calculation of ε from the Doppler spectrum width is subject to large uncertainties and careful analysis is needed. The situation is even worse for weather radar scanning azimuthally. On the one hand, for the vertically directed radar, the crossbeam wind, as well as the horizontal shear of the vertical air motion, can significantly contribute to the measured spectrum width and contaminate the turbulence measurement (Nastrom 1997; Chu 2002). Here we neglect the effect of the spread of the terminal velocities of the hydrometeors on the spectrum width since the clouds studied are non-precipitating and the vertical air motion dominates the spectrum width (Kollias et al. 2001; Lothon et al. 2005). On the other hand, for a beam directed at low elevation angles, Fang and Doviak (2008) show that an additional coupled term has been

neglected in the spectrum width equation heretofore. The coupled term is a zero mean random variable and affects the turbulence estimate as well. It is not clear if there is a coupled term in the spectrum width equation for the vertically directed radar beam too, but it is assumed here to also exist. For more detail of the coupled term, please refer to [Fang and Doviak \(2008\)](#). Both the cross-beam wind component and the coupled term closely relate to the radar beam width ([Nastrom 1997](#); [Fang and Doviak 2008](#)). Typically, the broader is the beam width, the larger is the cross-beam wind contribution and the fluctuation of the coupled term. The radar used to collect data in this study has an one way half-power beam width of 0.2° , and here we discuss the technique used to retrieve ε from the spectrum width and verify whether or not the fine angular resolution of the millimetre wavelength cloud radar is able to effectively limit the impacts from the cross-beam wind component and the coupled term.

The turbulence closure often involves the parametrization of a length scale (e.g. turbulence length scale, [Zeman and Tennekes 1977](#); dissipation length scale, [Stull 1988](#)) that allows for a relationship between the resolvable scale velocity variance and ε . Estimates of these length scales in stratocumulus clouds from observations are limited. The ε values retrieved from the millimetre wavelength cloud-radar measured spectrum width not only provides an opportunity to calculate the vertical integral length scale but also provides an opportunity to examine its time variability.

Coherent eddies have been characterized in several previous radar studies of stratocumulus clouds (e.g., [Ghate et al. 2010, 2011](#); [Mechem et al. 2010a](#)). These studies provide insight into the structure of elements that are explicitly resolved by large-eddy simulations (LES). In this study the characterization of large eddies is expanded to include the ε and radial velocity variance structure within updrafts and downdrafts. Since the ε distributions can interact with the supersaturation field within the updrafts, these interactions may be important in modulating drop-size distributions and drizzle-producing processes in stratocumulus clouds.

The following section discusses the technique used to retrieve the energy dissipation rate, ε . Section 3 presents the mean vertical structures of various parameters in cloud layer, and Sect. 4 investigates the time evolution of the vertical structures. Section 5 examines the coherent structures associated with large-eddies observed in the stratocumulus clouds and compares the structures observed during the day and at night. Section 6 provides a summary and conclusions.

2 Turbulence Retrieval Techniques

This section introduces the technique used to retrieve ε from the radar-measured spectrum width. To check the reliability of this technique, the resultant ε was also compared with ε calculated from the power spectra of the Doppler velocity. The characteristics of the associated Doppler velocity are described in detail in F13.

2.1 Calculation of ε from Power Spectra

A power spectrum is obtained from a time series of the Doppler velocities (vertical air velocities) at the same normalized height at which Doppler spectrum widths are observed. The normalized height has been defined as the height above cloud base normalized by the cloud depth (see F13). Although the normalized height is unique for all data in the same time series, the corresponding physical height may change from one time to the next. [Frisch et al. \(1995\)](#) showed that the fall velocity of a cloud droplet is negligible in a cloud with reflectivity below -17 dBZ. For the case studied here, the reflectivity is less than about

−20 dBZ as shown in Fig. 1b of F14. Thus the cloud particles are excellent tracers of air motions. Because of the very narrow beam of the millimetre wavelength cloud radar, the radar-measured radial velocity can be approximately considered as the vertical air velocity. However, this velocity is not that at a point but a volumetric mean velocity weighted by beam pattern and reflectivity. The contribution from the turbulence on scales smaller than the beam size has been significantly attenuated (Srivastava and Atlas 1974). The 16 h of radar observations used in this study are separated into 16 1-h length segments. In each segment, the 1-h mean velocity is calculated and subtracted from each instantaneous measurement at the same normalized height to isolate the turbulent component of the radial velocity. Fourier analysis of the isolated time series of the turbulent velocity and application of the horizontal advection wind speed obtained from wind-profiler measurements (see F14) at the Atmospheric Radiation Measurement program South Great Plains site gives the power spectrum in wavenumber space that is primarily due to the turbulence on scales larger than the radar beam size. Figure 1 shows an example of the power spectrum generated from data recorded between 1100 CST and 1200 CST at a normalized cloud height of 0.4. The black line is a least-square fit excluding wavelengths longer than about 950 m; the red line in Fig. 1 gives a least-square fit with the slope that is fixed to $-5/3$ and only the intercept changes to give the best fit. The red line is for reference purpose only, and is used to check the quality of the fitted line. If the fitted line (black) has a slope of $-5/3 \pm 0.2$, it is then used to compute the energy dissipation rate using

$$S(k_1) = A \varepsilon^{\frac{2}{3}} k_1^{-\frac{5}{3}} \quad (1)$$

where $S(k_1)$ is the spectral density at wavenumber k_1 and A is a dimensionless constant. For the one-dimensional transverse spectra shown in Fig. 1, $A = 0.2$ (Blackadar 1997, Sect. 9.4). The wavenumber is equal to the frequency obtained in Fourier analysis divided by the horizontal advection wind speed, i.e. $k_1 = f/\bar{u}$. Figure 2 shows a time series of the hourly median of the advection wind speed (solid line) and the 16-h median advection speed (dotted line) for the entire cloud layer. They are obtained from the wind profiler observations. Here we use median, not mean value, to eliminate possible outliers. There is a general decrease in the advection wind speed from about 8.5 m s^{-1} at the beginning of the observing period to a minimum of 3.5 m s^{-1} at 2330 (CST) and then an increase to 4 m s^{-1} during the last 1 h of observations. The hourly median values are used to transfer the power spectra from frequency domain to wavenumber domain for the results shown in Figs. 1 and 3. For comparison, the 16-h median advection speed, i.e. 5 m s^{-1} , was also used, but the results are degraded using a constant wind speed for the entire period.

2.2 Calculation of ε from Spectrum Width

Fang and Doviak (2008) show that the spectrum width equation for a scanning beam directed at low elevation angles is (i.e. their Eq. B13)

$$\overline{\sigma_v^2}^{(e)} = \sigma_\alpha^2 + \sigma_o^2 + \sigma_s^2 + \overline{\sigma_t^2}^{(e)} + T_c^{(e)}, \quad (2a)$$

where, σ_α , σ_o , σ_s , σ_t and T_c , represent the spectrum widths due to antenna rotation, hydrometeor oscillation and/or wobbling, shear of the mean wind, turbulence, and the coupled term due to coupling between shear and turbulence. The overbar denotes the spatial average weighted by the beam pattern and reflectivity; the superscript (e) signifies that the effective beam pattern must be applied for the scanning beam. A spectrum width equation through rigorous derivation and applicable to vertically directed beam does not exist. But, for the case

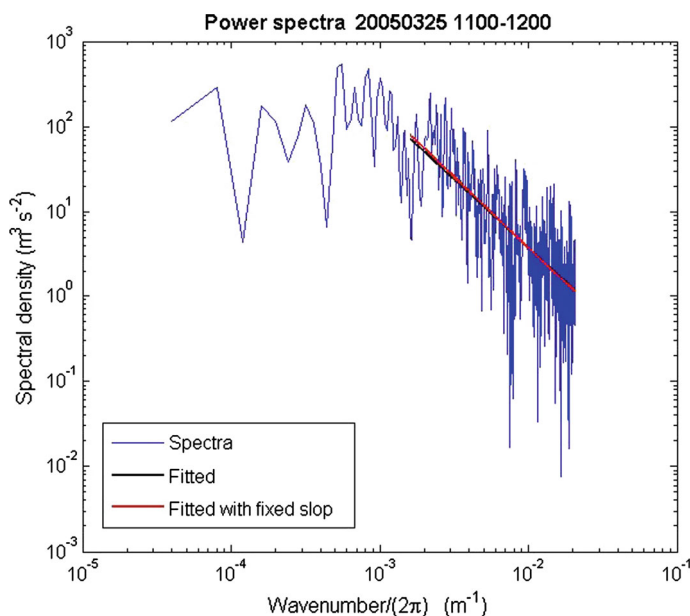


Fig. 1 Power spectra in clouds observed by the millimetre wavelength cloud radar at Lamont, Oklahoma. The black line is the least square fitting and the red line is fitted with a fixed $-5/3$ slope

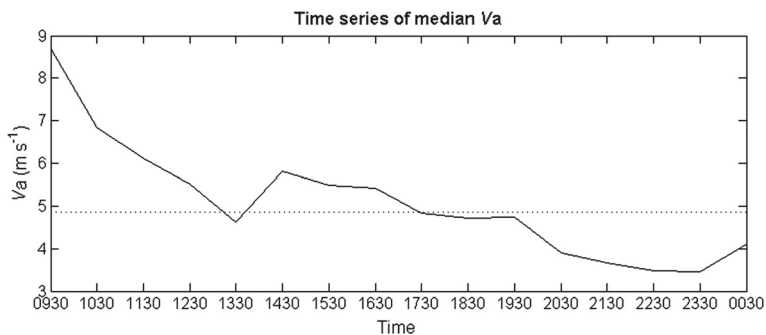


Fig. 2 Hourly median advection velocity (*solid*) and the 16-h median advection velocity (*dotted*) obtained for entire cloud layer from wind profiler observations

studied here, considering the stationary beam and the spread of the terminal velocities of the hydrometeors also contributing to the spectrum width and being independent from other contributors, the above equation can be rewritten as

$$\overline{\hat{\sigma}_v^2} = \overline{\sigma_s^2} + \overline{\hat{\sigma}_t^2} + \overline{\sigma_d^2} + T_c. \quad (2b)$$

Here, σ_a and the superscript (e) are dropped because the radar beam is stationary; the contribution due to the hydrometeor oscillation and/or wobbling is small and has been neglected; T_c remains and still represents the coupling between shear and turbulence. In addition to the vertical wind, the cross beam wind also contributes to the shear. Its contribution to the spectrum width has been included in σ_s because Eq. 1a is obtained in a spherical coordinate system. In non-precipitating stratocumulus clouds, hydrometeors are small and air motion

dominates (Frisch et al. 1995; Kollias et al. 2001) and the spectral width due to the spread of the terminal velocities of hydrometeors is small (Lothon et al. 2005). Thus σ_d can be neglected and Eq. 2b reduces further to

$$\overline{\hat{\sigma}_v^2} = \overline{\sigma_s^2} + \overline{\hat{\sigma}_t^2} + T_c. \quad (2c)$$

To isolate the turbulence contribution, $\overline{\sigma_s^2}$ needs to be removed. Here, only the contribution from the horizontal shear of the vertical wind is considered since the beam width of the millimeter wavelength cloud radar is so narrow that the contribution of the cross-wind to $\overline{\sigma_s^2}$ is negligible. From the radar-observed vertical velocity, one can compute the horizontal shear of the vertical velocity k_x using $k_x = \Delta v / (\bar{u} \Delta t)$ where Δv is the difference of the vertical velocity between two consecutive observations, \bar{u} is the horizontal advection wind speed and Δt is the cycle of two boundary-layer scanning modes of the cloud radar that is about 4 sec. The shear contribution, i.e. $\overline{\sigma_s^2}$ is (Doviak and Zrnic 1993)

$$\overline{\sigma_s^2} = k_x^2 \left(\frac{0.2h\pi}{180} + \bar{u} \Delta T \right)^2 / (16 \ln 2) \quad (3)$$

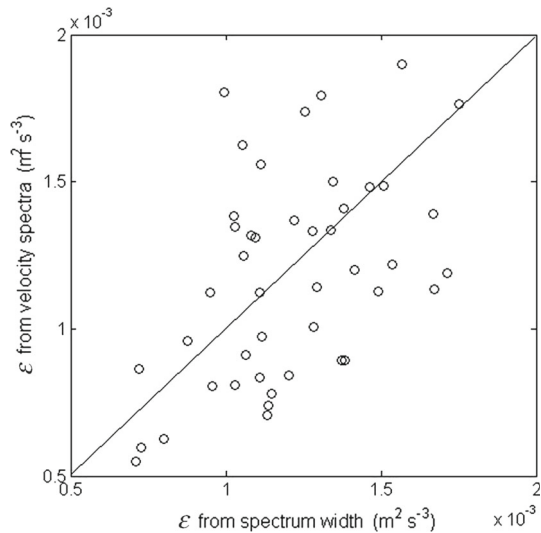
where 0.2 is the radar half-power beam width, h is the physical height of a range gate, and ΔT is the dwell time. In Eq. 3, the distance of an air parcel travelling in the dwell time has been taken into account. After subtracting $\overline{\sigma_s^2}$ from $\overline{\hat{\sigma}_v^2}$, one obtains $\overline{\hat{\sigma}_t^2} + T_c$. For two reasons, averaging the resultant $\overline{\hat{\sigma}_t^2} + T_c$ is necessary to obtain $E[\overline{\hat{\sigma}_t^2}] \approx \langle \overline{\hat{\sigma}_t^2} + T_c \rangle_t$ where $E[x]$ denotes the expectation of x and $\langle x \rangle_t$ denotes the time average. Firstly, the coupled term T_c is a random variable and contaminates the measurement of $\overline{\hat{\sigma}_t^2}$, although $E[T_c]$ is equal to zero. Secondly, the radar-measured Doppler spectrum is not an expected spectrum but an estimated spectrum and $\overline{\hat{\sigma}_t^2}$ calculated from this estimated spectrum is also a random variable fluctuating around its true value even without T_c . The average will reduce the impact of the coupled term and the fluctuation of $\overline{\hat{\sigma}_t^2}$ itself.

The resolution volume of the millimeter wavelength cloud radar is quite small. It is expected that the outer scale of the investigated turbulence is much larger than the radar-beam size and the turbulence significantly contributing to $\overline{\hat{\sigma}_t^2}$ is three-dimensional isotropic and falls within the inertial subrange. For this type of turbulence, based upon the work of Labitt (1981), Gossard and Strauch (1983) proposed an analytical expression to relate σ_{Π}^2 to ε as

$$\varepsilon = \frac{1}{\delta} \left[\frac{\sigma_{\Pi}^2}{1.35\alpha (1 - \gamma^2/15)} \right]^{3/2}, \quad (4a)$$

where $\sigma_{\Pi}^2 = \overline{\hat{\sigma}_t^2}$, which is the squared spectrum width due to turbulence only. Similar equations are also used (Doviak and Zrnic 1993; Chapman and Browning 2001; Kollias et al. 2005). However, Fang and Doviak (2008) and Fang et al. (2011) pointed out that the single $\overline{\hat{\sigma}_t^2}$ cannot be directly used to calculate ε , not only because T_c contaminates the measurement of $\overline{\hat{\sigma}_t^2}$ and $\overline{\hat{\sigma}_t^2}$ itself is a random variable, but also because the fact that Eq. 7 in Appendix B of Labitt (1981) is an ensemble average of $\overline{\hat{\sigma}_t^2}$, not a single value of $\overline{\hat{\sigma}_t^2}$. Thus, the above equation needs to be corrected as

Fig. 3 Scatter plot between ε calculated from power spectra and that calculated from the spectrum width. The slope of the solid line is 1



$$\varepsilon = \frac{1}{\delta} \left[\frac{\langle \hat{\sigma}_t^2 \rangle_t}{1.35\alpha (1 - \gamma^2/15)} \right]^{3/2}, \quad (4b)$$

where

$$\delta = a, \quad \gamma^2 = 1 - (b/a)^2, \quad \text{if } b \leq a \quad (4c)$$

or

$$\delta = b, \quad \gamma^2 \approx 4[1 - (b/a)^2], \quad \text{if } a \leq b \quad (4d)$$

and

$$a = r\sigma_\theta, \quad b = \sigma_r, \quad (4e)$$

$$\sigma_\theta = \theta_1 / (4\sqrt{\ln 2}), \quad \sigma_r = 0.35c\tau/2. \quad (4f)$$

Here, θ_1 is the one-way half-power beam width that is 0.2° for the millimeter wavelength cloud radar, c is the speed of light in air, τ is the pulse width, i.e. 0.3 ms for the data investigated here, r is the range from radar to a resolution volume. At 13 km, $a = b$, i.e., $a > b$ if $r > 13$ km and $a < b$ if $r < 13$ km. For our case, a is always $< b$ and therefore Eq. 4d is used to calculate ε from $\hat{\sigma}_t^2$. It is noteworthy that Eq. 4b cannot be reduced to Eq. 4a.

Figure 3 shows the scatter plot between ε calculated from the power spectra, i.e. $\varepsilon(w_t)$, where w_t is the turbulent component of the radial velocity, and those from the hourly median value of the spectrum width due to turbulence, i.e. $\varepsilon(\hat{\sigma}_t^2)$. There are 96 total samples at six normalized heights within 16 h, but some samples have been removed for power spectra that have the slopes beyond $-5/3 \pm 0.2$ on a log-log scale plot, such as that shown in Fig. 1. The values of $\varepsilon(w_t)$ fall between $0.6 \times 10^{-3} \text{ m}^2 \text{ s}^{-3}$ and $1.9 \times 10^{-3} \text{ m}^2 \text{ s}^{-3}$ whereas the values of $\varepsilon(\hat{\sigma}_t^2)$ fall between $0.6 \times 10^{-3} \text{ m}^2 \text{ s}^{-3}$ and $1.8 \times 10^{-3} \text{ m}^2 \text{ s}^{-3}$. These values agree well with the $10^{-3} \text{ m}^2 \text{ s}^{-3}$ mean value of ε in a cloudy boundary layer reported by Siebert et al. (2006) and the ε value in the inversion layer above a marine stratocumulus (Katzwinkel

Table 1 Some statistics between $\varepsilon(w_t)$ calculated from the velocity power spectra and $\varepsilon(\hat{\sigma}_t^2)$ calculated from the spectrum width

Mean $\varepsilon(w_t)$	Mean $\varepsilon(\hat{\sigma}_t^2)$	Mean $(\varepsilon(w_t) - \varepsilon(\hat{\sigma}_t^2))$	Std $(\varepsilon(w_t) - \varepsilon(\hat{\sigma}_t^2))$	R^2
$1.2 \times 10^{-3} \text{ m}^2 \text{ s}^{-3}$	$1.2 \times 10^{-3} \text{ m}^2 \text{ s}^{-3}$	$3 \times 10^{-5} \text{ m}^2 \text{ s}^{-3}$	$3.2 \times 10^{-4} \text{ m}^2 \text{ s}^{-3}$	0.37

et al. 2012). The values of both $\varepsilon(w_t)$ and $\varepsilon(\hat{\sigma}_t^2)$ are self-consistent during the entire 16-h observation time period. The solid line in Fig. 3 has a slope of 1; the closer the circles to the line, the better the agreement is between $\varepsilon(w_t)$ and $\varepsilon(\hat{\sigma}_t^2)$. The ratios between values of $\varepsilon(w_t)$ and $\varepsilon(\hat{\sigma}_t^2)$ fall between 0.6 and 1.6. Compared with previous studies where the ratio between $\varepsilon(\hat{\sigma}_t^2)$ and ε calculated from other methods could range over several orders of the magnitude, $\varepsilon(w_t)$ and $\varepsilon(\hat{\sigma}_t^2)$ in Fig. 3 agree well with each other. To further quantify the agreement between $\varepsilon(w_t)$ and $\varepsilon(\hat{\sigma}_t^2)$, Table 1 tabulates the mean values of $\varepsilon(w_t)$, $\varepsilon(\hat{\sigma}_t^2)$, $\varepsilon(w_t) - \varepsilon(\hat{\sigma}_t^2)$ and the standard deviation of $\varepsilon(w_t) - \varepsilon(\hat{\sigma}_t^2)$. It can be seen that mean $\varepsilon(w_t)$ and mean $\varepsilon(\hat{\sigma}_t^2)$ are equal. Moreover, compared with the mean of $\varepsilon(w_t)$ and $\varepsilon(\hat{\sigma}_t^2)$, the mean $\varepsilon(w_t) - \varepsilon(\hat{\sigma}_t^2)$ and its standard deviation are about two orders and one order of magnitude smaller respectively. These observations indicate that, overall or statistically, the two ε estimates agree well with each other. A Student's t test applied to this case also confirms this conclusion. However, the scatter plot in Fig. 3 shows low correlation between the two ε . The R^2 value in Table 1, i.e. 0.37, which is $\varepsilon(w_t)$ relative to the solid black line, is low too; the poor correlation may at least be attributed to five reasons: (1) when removing the contribution of the horizontal shear of the vertical wind to the radar-measured spectrum width, we assume the shear is linear. Considering that this assumption may not be necessarily true and the impact of the cross-beam wind has been neglected, the shear contribution may not be properly removed; (2) the neglected drop-size distribution may affect the isolation of the spectrum width due to the turbulence; (3) both methods calculating ε require turbulence to be three-dimensional isotropic, but this requirement may not be necessarily satisfied; (4) the neglected droplet's terminal velocity may impede the estimation of the turbulent velocity; (5) there are inherent uncertainties in ε estimates from the vertical velocity spectrum. Considering these uncertainties, the $R^2 = 0.37$ ($R = 0.61$) value may just be acceptable. The results shown here probably signify that the fine angular resolution of the radar effectively limits not only affect of the cross-beam wind but also, when combined with the spatial or time average, the coupled term on the spectrum-width measurement.

3 Mean Vertical Structures of Turbulence for 16 h of Observations

The 16-h period of observations allows us to examine the average vertical structures of the turbulence and the diurnal variation in those structures. The profiles of the median values of the hourly ε , the squared spectrum width, reflectivity, total variance and the vertical integral length scale are shown in Fig. 4. As stated previously, the spectrum width and therefore ε calculated from the spectrum width at a single range gate is a random variable fluctuating around its true value. To obtain meaningful results, it is necessary to average a few measurements or to use the median value of a number of observations. Again, we use the median value to remove possible outliers that may affect the average. The hourly ε is calculated from the hourly median value

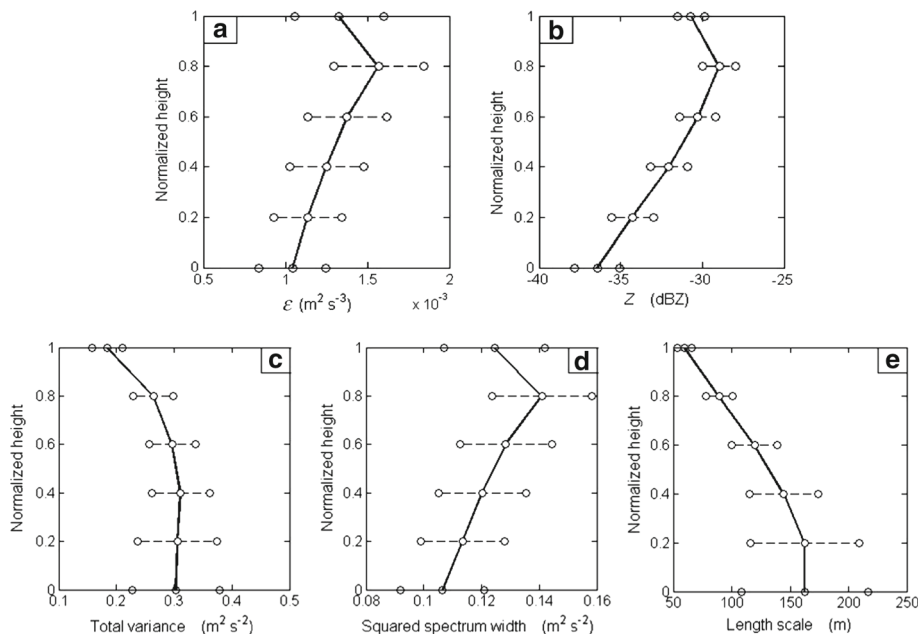


Fig. 4 Profiles of median ε (a), Z (b), total variance (c), squared spectrum width (d), and vertical integral length scale (e) over 16 h. Circles are one standard deviation from associated median values

of $\overline{\sigma_t^2}$, where the hourly total variance is the sum of the hourly variance of radial velocity and the hourly median of the squared spectrum width. It comprises the turbulence contribution from all scales (Rogers and Tripp 1964). The total variance is denoted as σ_w^2 , where σ_w is the standard deviation. The hourly vertical integral length scale is calculated using the hourly value of σ_w with $l_w = \sigma_w^3 / \bar{\varepsilon}$ where $\bar{\varepsilon}$ is the hourly mean. The ordinate in Fig. 4 represents the normalized height where 1 is cloud top and zero is cloud base. The circles on horizontal bars in Fig. 4 span one deviation away from the median values.

As shown in Fig. 4a, ε increases with height and reaches a maximum at normalized cloud depth=0.8 and then decreases. Cloud-top cooling drives both small-scale and large-scale turbulence, but some small-scale turbulence may dissipate in the process of being transported towards cloud base. The increase of ε below cloud depth=0.8 could partly reflect that the closer the proximity to the turbulence source, the stronger is the unresolved turbulence. It is interesting that the reflectivity shown in Fig. 4b has a vertical structure very similar to that of ε . This similarity or correlation between ε and reflectivity profiles signify that the increase in ε with height might partly be attributed to the increase of latent heating generated by condensation in the cloud layer. The reduced ε and reflectivity above cloud depth=0.8 may indicate that the entrainment zone is within the top 20 % of the cloud layer (about 100 m in depth). Here, the entrainment zone is defined as the region where mixing occurs between cloudy air and free atmosphere air. The actual thickness of the entrainment zone may be even smaller, but the vertical resolution of the radar measurements prevents a finer definition. One possible reason for the decreasing reflectivity and the EDR is that the entrainment and mixing in this zone dilutes the liquid water content of the cloud, as well as evaporates cloud droplets and suppresses the turbulence; another possible reason is that the radar resolution volume is only partially filled.

Shown in Fig. 4c is the total variance; unlike ε and the spectrum width that increases with height below cloud depth=0.8, the total variance is nearly a constant in the lower part of the cloud and decreases from a normalized height=0.4 up to cloud top. This difference is due to the lack of larger eddies at higher levels. A similar structure was also observed by Rémillard et al. (2012) in marine boundary-layer stratocumulus clouds. This structure is the combined result of the impact from cloud-top cooling and surface heating that is much stronger over land than that over the ocean. This distribution is consistent with the LES results of Zhu et al. (2010) for the same case studied here and the results of Mechem et al. (2010b) for continental stratocumulus clouds at the top of the boundary layer, and the climatology of continental stratocumulus clouds of Ghate (2009). Here the maximum $\sigma_w \approx 0.56 \text{ m s}^{-1}$ appears at cloud depth=0.4 and is about 0.54 of the mean total convective velocity scale W_t^* (see F14) for the entire time period and close to values found in previous modelling and observational studies (e.g. Deardorff 1980a; Nicholls 1984).

Shown in Fig. 4d is the squared spectrum width, which mirrors that of ε , which is calculated from the spectrum width. At cloud base, the squared spectrum width contributes about 40 % to the total variance. At the normalized height of 0.8 its contribution increases to about 50 % and to almost 70 % near cloud top. Its vertical distribution is very similar to the vertical distribution of the reflectivity. These observations signify again that the entrainment induced by cloud-top cooling and the latent heating due to liquid water condensation determine the squared spectrum width or the turbulence at scales smaller than the radar-beam size.

In Fig. 4e, the vertical integral length scale decreases from a maximum of about 160 m at cloud base to a minimum of 60 m at cloud top, indicating that relatively small-scale turbulence dominates near cloud top and large-scale turbulence dominates near cloud base. This is consistent with the observations obtained from Fig. 4d and also consistent with the observations obtained in F14 as well as supporting the observed difference between the vertical distributions of the total variance and ε . The integral length scales derived from LES shown by Bretherton and Park (2009) for nocturnal stratocumulus are similar in magnitude to those for the radar-derived estimates, but show more variability in the length scale near cloud top.

4 Diurnal Evolution of Vertical Structures

Compared with that over the ocean, the underlying surface heating is stronger over the land during the day and its diurnal variability is high and therefore its impact on surface fluxes and subsequently the cloud turbulence is more complex. This section represents the diurnal cycles of the mean vertical turbulence structures. The mean turbulence structures are calculated for four different time periods to illustrate how the in-cloud turbulence responds to the temporal variability of the forcing mechanisms. An analysis of the temporal evolution of surface forcing and the cloud-top forcing is shown in F14. The four time periods used here are labeled as: (1) DAY (1200–1500 CST) when the surface forcing is strongest and solar absorption in the cloud suppresses the cloud-top longwave radiative cooling, (2) EVENING (1700–2000 CST) when the surface forcing is near zero and upper-level clouds suppress the cloud-top longwave cooling at cloud top, (3) NIGHT (2000–2300 CST) when there is strong longwave cooling at cloud top at around 2200 CST when clouds overhead reduce the cooling, and (4) MIDNIGHT (2300–0100 CST) when longwave cloud-top radiative forcing is high. The mean vertical structure for these four time periods are again characterized using radar reflectivity, total vertical velocity variance, squared spectrum width, the eddy dissipation rate calculated from the spectrum width and the vertical integral length scale, which is often

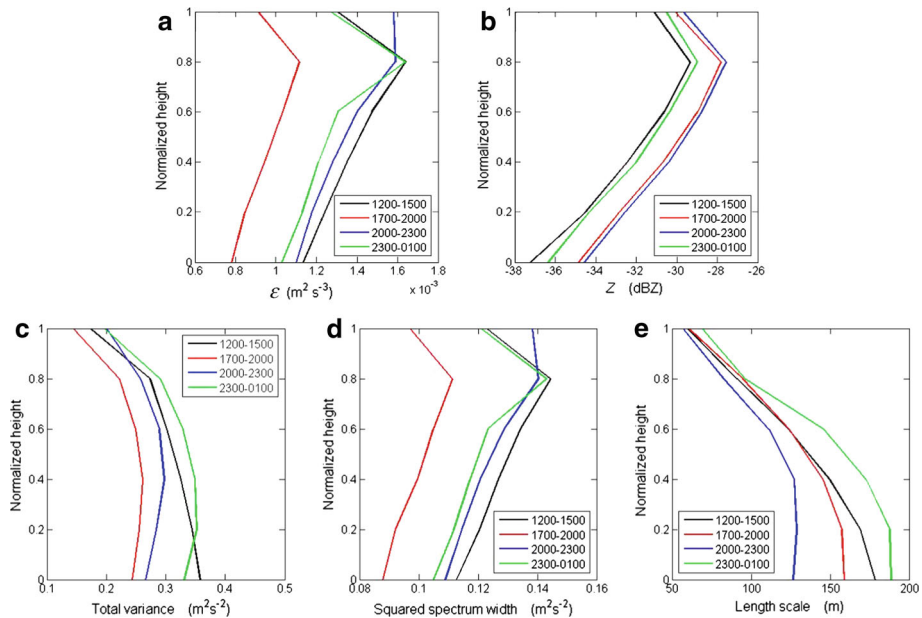


Fig. 5 Profiles of median ε (a), Z (b), total variance (c), square spectrum width (d) and vertical integral length scale (e) for the four time periods discussed in the text

Table 2 Mean values of cloud depth (CD), liquid water path (LWP) and other variables during four time periods for entire cloud layer

Time	$CD(\text{m})$ $\pm \sigma$	LWP (g m^{-2})	W_t^* (m s^{-1})	σ_{vr} (m s^{-1})	σ_{vr}/W_t^*	$\sqrt{\langle \hat{\sigma}_t^2 \rangle_t}$ (m s^{-1})	$\sqrt{\langle \hat{\sigma}_t^2 \rangle_t}/W_t^*$	$\langle \hat{\sigma}_t^2 \rangle_t/\sigma_w^2 \times 100\%$
1200–1500	268 ± 37	108.8	1.21	0.42	0.35	0.36	0.30	42
1700–2000	228 ± 55	97.6	0.57	0.37	0.65	0.32	0.56	43
2000–2300	240 ± 64	88.7	0.99	0.38	0.38	0.35	0.35	46
2300–0100	222 ± 46	90.3	1.18	0.43	0.36	0.35	0.30	40

used in turbulence closure. As mentioned previously, the total vertical velocity variance is estimated as the sum of the variance of the radar-measured radial velocity and the squared spectrum width. Thus, in addition to the profiles and evolution of those variables, we are able to examine the relative contribution of the unresolved turbulence to the total variance.

The profiles of the median values of ε , squared spectrum width, reflectivity, total variance and the vertical integral length scale for the four time periods are shown in Fig. 5. Table 2 tabulates the mean values of cloud depth \pm the standard deviation, liquid water path, W_t^* , σ_{vr} (standard variation of radial velocity) the ratios σ_{vr}/W_t^* , $\sqrt{\langle \hat{\sigma}_t^2 \rangle_t}/W_t^*$ and $\langle \hat{\sigma}_t^2 \rangle_t/\sigma_w^2$ for the four time periods for the entire cloud layer. It can be seen that ε , total variance and squared spectrum width are high in the DAY period when the surface heating

is strong and lowest in the EVENING period when solar radiation is zero and the cloud-top cooling is reduced by upper-level clouds so that the mean W_t^* is at its minimum, as shown in Table 2. Although the cloud-top cooling is weak and surface heating diminishes, the longwave warming at cloud base is still present, which may combine with the weak cloud-top cooling to reduce the in-cloud turbulence decay during this time period (see Fig. 4 of F14). From the EVENING to the MIDNIGHT period, with the increase of the cloud-top longwave radiative cooling, turbulence is intensified. Then, ε , total variance and squared spectrum width in the NIGHT period are higher than those during the EVENING period. During the MIDNIGHT period, the total variance is highest at all levels except near cloud base although the mean W_t^* is lower than that during the DAY period and ε and the squared spectrum width are reduced below the normalized height of 0.8. Furthermore, considering that there are two decoupled mixing layers below clouds as shown in Fig. 3 of F14 and surface heating may be unable to affect the turbulence in the clouds (F14), the highest turbulence levels during this time period may signify that the substantially intensified cloud-top cooling effectively drives the even stronger turbulence. This deduction is supported by the increased value of σ_{vr} during the MIDNIGHT period in Table 2. The highest variance values and relatively lower W_t^* during this time period may also imply that the cloud-top radiative cooling is more efficient in forcing turbulence. Compared with those values around noon, ε , the total variance and the squared spectrum width are relatively greater in the upper part of the cloud during the NIGHT period than during the DAY period when the cloud-top cooling is reduced; although ε and the squared spectrum width decrease to the level of the DAY period in the MIDNIGHT period, the total variance is the highest, which implies that the turbulence near cloud top with scales larger than the radar resolution volume is stronger than that in other time periods.

During the day and night the maximum reflectivity is observed persistently at the normalized height of 0.8 where the ε maximum also appears. Compared with those during the day, the reflectivity factor is about 1.5 dBZ higher at all levels during the EVENING and NIGHT periods, except during the MIDNIGHT period when the reflectivity is similar to that observed during the day. The relatively higher turbulence during the DAY and MIDNIGHT may cause relatively stronger entrainment that dilutes water content in cloud and leads to relatively lower reflectivity.

The vertical integral length scale profiles (Fig. 5e) all show a decrease with height with the length scale near cloud top at about 60 m compared with the 130–180 m length scales near cloud base. The temporal variations in the vertical length scale near the cloud top are small, but are substantial at the lower part of the cloud. The distribution of the vertical length scale during the MIDNIGHT period indicates that the radiative cooling from cloud top, maybe combined with other forcing such as latent heating due to the water vapour condensation, drives small-scale turbulence near cloud top and larger-scale turbulence near cloud base when cold air sinks and is accelerated by gravity. This deduction is consistent with that obtained in F14 and could at least partly explain why ε and the squared spectrum width are relatively lower below the normalized height of 0.8 during this time period.

From Table 2, the percentages of the squared spectrum width relative to the total variance [i.e. $(\langle \hat{\sigma}_t^2 \rangle_t / \sigma_w^2) \times 100 \%$], vary only from 40–46% and indicate that, at all times, the unresolved turbulence is equally important as the resolved turbulence. A similar conclusion can be obtained by checking $\sqrt{\langle \hat{\sigma}_t^2 \rangle_t} / W_t^*$ and σ_{vr} / W_t^* in the same Table.

Based upon the observations presented above, we may further conclude that the cloud-top radiative cooling is equally as important as the underlying surface heating in driving turbulence in this continental stratocumulus case. Sometimes it might be the unique contributor,

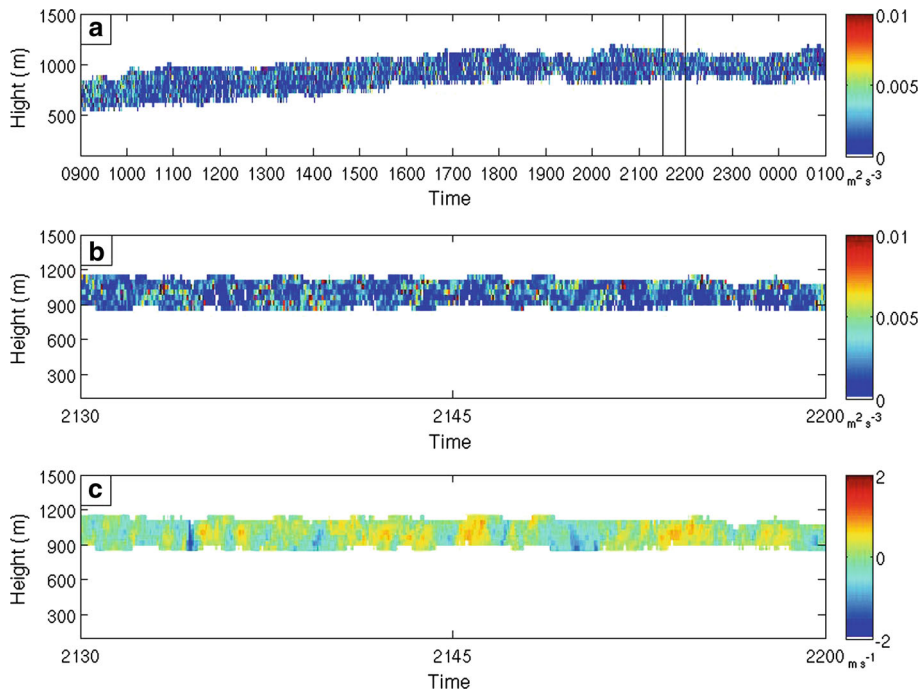


Fig. 6 Time-height display of 16-h ε values (a), 30-min ε (b), and 30-min radial velocity (c). The *black box* in the top panel indicates the 30-min time window in which the ε and radial velocity are shown in the middle and bottom panels

as in the MIDNIGHT period when surface heating is unable to affect in-cloud turbulence because it is weaker and decoupling occurs below cloud base. It also appears that the warming at cloud base can contribute to the turbulence budget. In Table 2, from evening to night, W_t^* changes significantly but σ_w , which is the square root of the sum of squared σ_{vr} and squared spectrum width, is nearly unchanged. This indicates that other external forcings such as latent heating/cooling related to the water vapour condensation and cloud droplet evaporation, and wind shear, may also need to be included in W_t^* to obtain a better relation between W_t^* and σ_w .

5 Coherent Structures of Vertical Velocity and Eddy Dissipation Rate (ε)

The use of the spectrum width allows the ε to be estimated for the entire time period and at the same resolution as the radar observations. Figure 6a shows the ε field for the entire 16-h period, and Fig. 6b, c shows the 30-min high-resolution ε values and radial velocity between 2130 CST and 2200 CST that allow us to investigate the relationships between air motions and patterns in the ε field. Here, ε at each radar range gate is calculated from individual $\hat{\sigma}_t^2$. Since the second moment of the radar Doppler spectrum is a noisy estimator, especially at low signal-to-noise conditions, and is sensitive to non-uniform beam filling conditions, the ε value at each radar range gate is expected to be highly variable (Gossard et al. 1998). Furthermore, even in high signal-to-noise conditions and without non-uniform

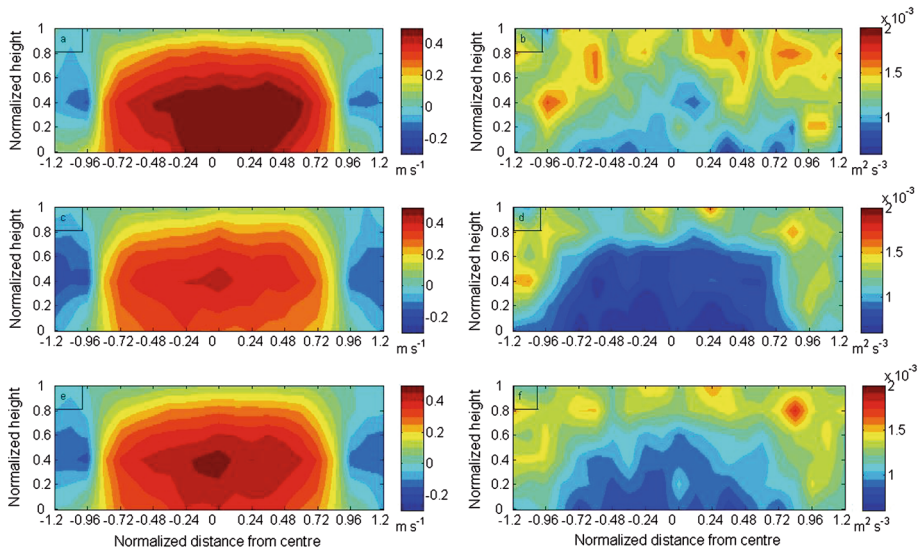


Fig. 7 Coherent structures of the vertical velocity (*left panels*) and the ε values (*right panels*) in updraft region during the day (**a**, **b**), night (**c**, **d**), and for entire 16-h (**e**, **f**)

beam filling issues, the individual spectrum width and therefore ε calculated from it are still random variables fluctuating around their true values (Fang and Doviak 2008). However, the availability of ε with high spatial and temporal resolution allows the identification of recognizable and meaningful patterns even though the ε field is noisy. An example of an updraft core can be observed around 2146 CST, starting from cloud base and extending through the cloud layer to the cloud top. An area of low ε can be observed in this updraft area. The high ε values appear on the top and edges of the updraft and form a bell-shape boundary surrounding the lower ε area. This pattern indicates that the flow in the updraft core is more laminar. There are more than four similar structures in the 30-min time window. In contrast to the updraft cores, the downdraft areas often have high ε values and the air motion is more turbulent. It can be seen that the vertical and horizontal dimensions of these high or low ε areas change from case to case.

To investigate the coherent structures associated with large-eddy updrafts and downdrafts in detail, a two-dimensional normalized coordinate system is used. The ordinate is the same as that defined in F13. The abscissa represents the distance of a point from the geometric centre of an updraft or downdraft region normalized by the half width of the region; the negative and positive signs indicate the past or future time relative to the centre respectively. An updraft region is defined as a region where its width at a normalized height of 0.4 is at least 200 m or 10 consecutive observations and air moves upward over the entire region at the same normalized height; a downdraft region is defined in a similar way, but downward motion at a normalized height of 0.6 is used as an indicator. Within the entire observing period (16 h) investigated, there are 217 updraft regions and 206 downdraft regions that were selected by application of the updraft and downdraft criteria. The width of the largest updraft region is about 1180 m and the width of the largest downdraft region is about 1240 m. The mean width is about 330 m for updrafts and 300 m for downdrafts.

Shown in Fig. 7 are the vertical velocity and the ε mean coherent structures around the updraft. The upper panels show structures observed during the daytime; the middle pan-

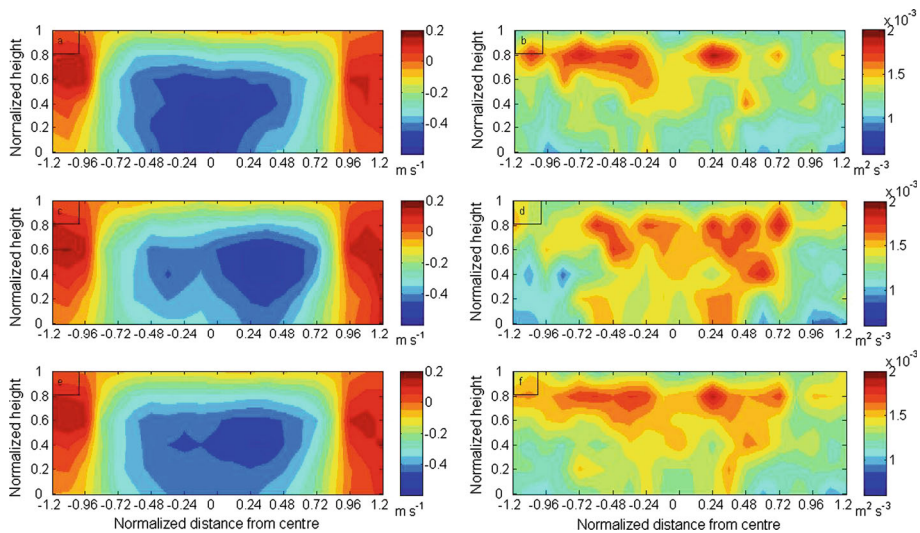


Fig. 8 Similar to Fig. 7 but in the downdraft region

els show the structures observed during the nighttime, and the bottom panels are the averaged structures for the entire 16-h period. Using the normalized distance from the centre of the updraft structures implies that the wider structures have been compressed whereas the narrower structures have been expanded. By definition the updraft region is located between -1 and 1 at a normalized height of 0.4 . For the 16-h mean structure, the updraft starts from cloud base and extends up to a normalized height of about 0.6 and decelerates above due to the stability of the inversion layer at cloud top. Because of the surface heating, the updraft is more vigorous during the day than at night. The updraft core is more laminar at night and more turbulent in the day. The larger ε values always appear on the top and along the edges of the updraft core and form a bell shape surrounding the core.

One may argue that the larger ε values at the edges of the updraft are not due to stronger turbulence but due to the horizontal shear of the vertical wind; but we have sufficient arguments to exclude this possibility. First, as indicated previously, we have designed and implemented an algorithm to remove the shear contribution from the radar-measured spectrum width. This shear-removal algorithm could fail to work when the interface between the updraft and downdraft falls in a single radar resolution volume. In such a case, the large ε values will appear around the interface, but this correlated pattern does not appear in Fig. 7. Secondly, a large shear area could coincide with a large ε area too since shear contributes to the production of turbulence. Thus, it is not possible to attribute the large estimated ε in a large shear area to shear and not to turbulence. Finally, if the large ε values are due to the inside-beam shear, they should not only appear at the updraft edges but also at the downdraft edges, but this feature is not seen, as will be discussed in the next section.

The coherent structures of the downdraft during daytime, nighttime and the entire observing period in the normalized coordinate system are shown in Fig. 8. For the 16-h mean structure, in the upper portion of the downdraft, the downward air velocity decreases with height. This indicates that air sinks from the cloud top and accelerates. The downdraft core

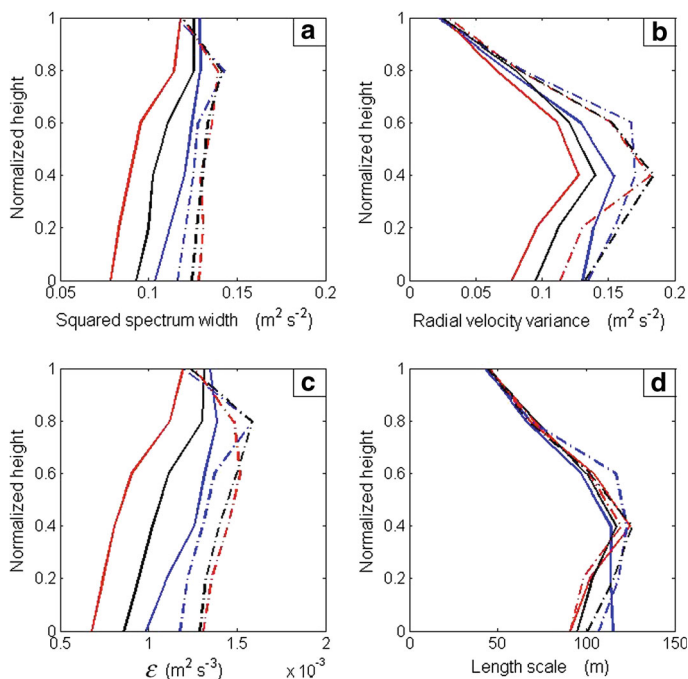


Fig. 9 Vertical structures of the squared spectrum width (**a**), radial velocity variance (**b**), ε (**c**), and the integral length scale (**d**) in updraft (solid lines) and downdraft (dashed-dotted lines) during the day (blue), night (red) and the entire 16-h time period (black)

extends from the middle to the bottom of the cloud during the day, but reaches a maximum in the middle of cloud at night. This behaviour seems to contradict the observation that the surface heating is stronger in the day; but it is consistent with the mass continuity requirement since the updraft core exhibits the similar structures. The retrieved ε values are higher during the night and lower during the day. Compared with conditions in the updraft, the turbulence is more intense in the downdraft core than in the surrounding areas. This feature is even more prominent during the night. The turbulence in the downdraft core is stronger than that in updraft core, which indicates that the updraft core is more closely laminar and the downdraft core is more turbulent; these observations may reflect turbulent circulations that are primarily driven by sinking air due to the cloud-top radiative cooling. We speculate that the cloud-top cooling may give rise to smaller-scale eddies near cloud top that may be embedded within the larger eddies that circulate through the entire boundary layer (or cloud layer). A strong layer of turbulence appears in both the updraft and downdraft around the normalized height of 0.8 where the air is either accelerated or decelerated. The strongest reflectivity also appears around that height as shown in Fig. 5b. As mentioned previously, high ε values due to strong inside-beam shear are not observed at the downdraft edges. The diurnal variation of ε in the updraft is more prominent than that in the downdraft. The persistent high ε in the downdraft core may again reflect the fact that the in-cloud turbulence circulation is driven primarily by the downdraft during the day and the night.

To further investigate the coherent structures and the embedded turbulence, the mean vertical structures of the squared spectrum width, the radial velocity variance of perturbations relative to the 1-h means, the ε values and the vertical integral length scale in the updraft

and the downdraft were calculated and are shown in Fig. 9. For the entire 16-h time period, the profiles of the squared spectrum width and ε in both updrafts and downdrafts all show a slight increase with height below a normalized cloud depth of 0.8; above this level the variations of the squared spectrum width and ε in the updraft is negligible, but a sharp decrease can be observed in the downdraft. Both the squared spectrum width and ε are higher in the downdraft except near the cloud top. Moreover, the squared spectrum width and ε show a larger diurnal variation in the updraft than in the downdraft, and are greater during the day in the updraft, but greater at night in the downdraft below a normalized cloud depth of 0.7 and near cloud top. The opposite behaviour is observed between cloud depth of 0.7 and 0.9; however, the changes near cloud top in the downdraft are negligible. These results confirm the previous observations and disclose even more detailed vertical structures. Furthermore, these results indicate that both cloud-top radiative cooling and surface heating contribute to the small-scale turbulence in the updraft and the downdraft during the day, but the impact of the surface heating on the small-scale turbulence in the updraft is more prominent. Near the cloud top in the downdraft, the influence of the surface heating on the small-scale turbulence is negligible. The reduced small-scale turbulence intensity during the day in the downdraft below cloud depth=0.7 may be attributed to the reduced radiative cooling at cloud top due to absorption of solar radiation. The vertical structure of the radial velocity variance differs from the vertical structures of the squared spectrum width and ε . For the 16-h mean structures in both updrafts and downdrafts, ε slightly increases with height from the cloud base and peaks at a normalized height of 0.4 and then decreases. Similar to the squared spectrum width and ε , the radial velocity variance in the downdraft is higher, which indicates that the large-scale or resolved-scale turbulence is stronger in the downdraft than that in the updraft; the diurnal variation of the radial velocity variance is higher in the updraft.

The surface heating significantly contributes to the large-scale turbulence in the updraft during the day, but this contribution decreases with height and diminishes to the cloud top. The relatively lower variance in the downdraft during the night indicates that surface heating also significantly contributes to the large-scale turbulence in the downdraft in the lower part of the cloud during the day. During the day, in the downdraft area, the surface heating combined with the cloud-top radiative cooling creates a strong large-scale turbulence layer between a normalized height of 0.4 and 0.6; above cloud depth=0.6 the influence of the surface heating is negligible. The negligible variations of the radial velocity variance near the cloud top in both updraft and downdraft indicate that the large-scale turbulence near cloud top is dominantly driven by the cloud-top radiative cooling.

The vertical integral length scales all have a vertical structure very similar to the radial velocity variance except in the lower part of the cloud in the updraft during the day. They are about 90–110 m at cloud base, increase with height to a maximum at cloud depth=0.4 and then decrease to about 40 m at the cloud top. During the day in the updraft, the vertical length scale is about 120 m persistently from the cloud base to cloud depth=0.4. These observations signify that the small-scale turbulence dominates near cloud top whereas larger scale turbulence dominates near cloud base in both the updraft and downdraft and are consistent with the observations shown previously. The length scale profiles are similar for both updrafts and downdrafts and under different forcing conditions. The length scales shown in Fig. 9a are smaller than those observed for the 1-h variances shown in Fig. 5e, since the large-eddy variance has been removed. But the collapse of these scales to similar profiles indicates the validity of using these length scales for parametrizing eddy dissipation rates in models that explicitly resolve the larger eddies.

6 Summary and Conclusions

Observations from a millimetre wavelength cloud radar located at the Atmospheric Radiation Measurements program Southern Great Plains site are used to examine the turbulence structure within a continental stratocumulus cloud layer that appears atop the boundary layer. The observations cover 16 h following the passage of a cold front. The radar-measured spectrum width provides the characteristics of the small-scale turbulence. It is shown that ε calculated from the hourly median value of spectrum width agrees well with that calculated from velocity power spectra. This good agreement implies that, 1) the narrow beam of the radar can effectively limit the impact of the cross-beam wind on the spectrum width measurements; 2) the narrow beam combined with the use of the median value of the spectrum width can effectively reduce the impact of the coupled term; 3) in non-precipitating stratocumulus clouds the cloud drop terminal velocity is negligible; and 4) the shear-removing algorithm used in this study is sufficient. The magnitude of ε obtained herein agrees well with the mean value of $10^{-3} \text{ m}^2 \text{ s}^{-3}$ in a cloudy boundary layer reported by Siebert et al. (2006). It also agrees well with the energy dissipation rate in the inversion layer above a marine stratocumulus (Katzwinkel et al. 2012).

The vertical distribution of ε in the cloud layer is attributed to the cloud-top cooling and the condensation latent heating increasing with height. The relatively lower ε and reflectivity above a normalized cloud depth=0.8 results from the cloud droplet evaporation and the diluted cloud water content due to entrainment and mixing between cloudy air and drier free atmospheric air. The contribution of the squared spectrum width to the total variance substantially increases with height and signifies that the unresolved turbulence more closely relates to the entrainment induced by cloud-top cooling. This is consistent with the decrease of the mean vertical integral length scale with height and indicates that small-scale turbulence dominates near cloud top and large-scale turbulence dominates near cloud base.

In the entire cloud layer, the squared spectrum width contributes about 40–46 % of the total variance and therefore the unresolved turbulence is as important as the resolved turbulence. Both the cloud-top cooling and the surface heating are important in driving the in-cloud turbulence during the day whereas the cloud-top cooling predominates during the night. During the day, the solar radiation heating balances the longwave radiative cooling and suppresses the turbulence development near cloud top; during the night, the strongly intensified cloud-top cooling drives not only the unresolved turbulence but also the resolved turbulence that has length scales \leq the cloud depth. Unlike in marine stratocumulus the in-cloud turbulence is of high intensity during the day and lowest around sunset at all levels, and increases during the night with the intensification of the cloud-top cooling.

The composite coherent structure of updrafts is characterized by low ε in the updraft core. Larger ε values surround the updraft core and appear at the top and at edges. In the updraft of these continental stratocumulus clouds, the turbulence is weaker at night and stronger during the day. In contrast to that in the updraft, ε is large inside the downdraft core and low in the surrounding areas. Compared with the updraft, the downdraft is more turbulent. The cloud-top cooling may give rise to smaller-scale eddies within the larger eddies that are characterized by the coherent updraft and downdraft structures. Opposite to that in the updraft, the turbulence in the downdraft is stronger at night and weaker during the day. For both updraft and downdraft, the maximum ε occurs at a normalized height ≈ 0.8 where reflectivity is a maximum and the acceleration or deceleration is observed. If similar turbulence structures in coherent eddies exist in deeper clouds, it may be possible that the enhanced ε at the top of updrafts may enhance collision and coalescence in this area and promote drizzle production

near cloud top. Likewise the enhanced ε in the downdrafts, particularly at night, may enhance precipitation production in these areas.

In both updrafts and downdrafts, the radial velocity variance (the resolved turbulence) in the mean vertical coherent structures differs from the squared spectrum width (unresolved turbulence) in a manner similar to that observed in marine stratocumulus (Wood 2012). The resolved turbulence is stronger in the downdraft. The larger diurnal variation in the updraft indicates the impact of the surface heating on the large-eddy structures, with the effects of surface heating decreasing with height. The negligible variation of the radial velocity variance near cloud top in both updrafts and downdrafts indicates that the resolved turbulence around cloud top is mostly due to the cloud-top cooling; but lower in the cloud layer both cloud-top cooling and surface heating contribute to the generation of the resolved turbulence during the day.

The spectrum width at a single range gate, or ε calculated from it, is a random variable fluctuating around its true value, but the high spatial and temporal resolution observations from the millimeter wavelength cloud radar allow us to establish meaningful patterns through averaging. This study illustrates the utility of using Doppler spectrum width from the millimeter wavelength cloud radar to calculate ε and thus investigate processes involved in the turbulence structure of stratocumulus clouds. The observed temporal variability can be used to examine the transient response of LES to changes in the surface and cloud-top forcing. Further, it allows for the possibility of comparing the simulated turbulence characteristics from LES models with those obtained from the cloud-radar observations. The vertical length scale inferred from these observations can be used to evaluate subgrid parametrizations used in numerical models operating on a variety of scales and aid in the development of parametrizations of dissipation rates as a function of the resolvable-scale vertical velocity variance in some classes of numerical model.

Acknowledgments This research was supported by the Office of Biological and Environmental Research (BER) of the U.S. Department of Energy under Grant DE SC 0000777 and 0008599 and was made possible by the measurement from the Atmospheric Radiation Measurement Climate Research Facility at the Southern Great Plains. We benefited from useful discussions with Dr. Christopher Fairall.

References

- Blackadar AK (1997) Turbulence and diffusion in the atmosphere. Springer, New York, 195 pp
- Bouniol D, Illingworth AJ, Hogan RJ (2003) Deriving turbulent kinetic energy dissipation rate within clouds using ground based 94 GHz radar. Preprints. In: 31st Conference on radar meteorology, Seattle, WA, American Meteorological Society, pp 193–196
- Bretherton CS, Park S (2009) A new moist turbulence parameterization in the community atmosphere model. *J Clim* 22:3422–3448
- Brewster KA, Zrnić DS (1986) Comparison of eddy dissipation rates from spatial spectra of Doppler velocities and Doppler spectrum widths. *J Atmos Oceanic Technol* 3:440–452
- Chapman D, Browning KA (2001) Measurement of dissipation rate in frontal zones. *Q J R Meteorol Soc* 127:1939–1959
- Chu Y (2002) Beam broadening effect on oblique MST radar Doppler spectrum. *J Atmos Oceanic Technol* 19:1955–1967
- Deardorff JW (1980a) Stratocumulus-capped mixed layers derived from a 3-dimensional model. *Boundary-Layer Meteorol* 18:495–527
- Doviak RJ, Zrnić DS (1993) Doppler radar and weather observations. Academic Press, San Diego, 453 pp
- Fang M, Doviak RJ (2008) Coupled contributions in the Doppler radar spectrum width equation. *J Atmos Oceanic Technol* 25:2245–2258
- Fang M, Doviak RJ, Albrecht BA (2011) Significance of the coupled term in the Doppler weather radar spectrum width equation. *J Atmos Oceanic Technol* 28:539–547

- Fang M, Albrecht BA, Ghaté VP, Kollias P (2014) Turbulence in continental stratocumulus, part I: External forcings and turbulence structures. *Boundary-Layer Meteorol*. doi:[10.1007/S10546-013-9873-3](https://doi.org/10.1007/S10546-013-9873-3)
- Frisch AS, Lenschow DH, Fairall CW, Schubert WH, Gibson JS (1995) Doppler radar measurements of turbulence in marine stratiform cloud during ASTEX. *J Atmos Sci* 52:2800–2808
- Ghaté VP (2009) Turbulence and mass-transports in stratocumulus clouds. A Dissertation, University of Miami, 124 pp
- Ghaté VP, Albrecht BA, Kollias P (2010) Vertical velocity structure of non-precipitating continental boundary layer stratocumulus clouds. *J Geophys Res* 115:D13204. doi:[10.1029/2009JD013091](https://doi.org/10.1029/2009JD013091)
- Ghaté VP, Miller MA, DiPretore L (2011) Vertical velocity structure of marine boundary layer trade wind cumulus clouds. *J Geophys Res* 115:D23201. doi:[10.1029/2010JD015344](https://doi.org/10.1029/2010JD015344)
- Gossard EE, Strauch RG (1983) Radar observation of clear air and clouds. Elsevier, New York, 280 pp
- Gossard EE, Wolfe DE, Moran KP, Paulus RA, Anderson KD, Rogers LT (1998) Measurement of clear-air gradients and turbulence properties with radar wind profilers. *J Atmos Oceanic Technol* 15:321–342
- Istok MJ, Doviak RJ (1986) Analysis of the relation between Doppler spectral width and thunderstorm turbulence. *J Atmos Sci* 43:2199–2214
- Katzwinkel J, Siebert H, Shaw RA (2012) Observation of a self-limiting, shear-induced turbulent inversion layer above marine stratocumulus. *Boundary-Layer Meteorol* 145:131–143
- Kollias P, Albrecht BA, Lhermitte R, Savtchenko A (2001) Radar observations of updrafts, downdrafts, and turbulence in fair-weather cumuli. *J Atmos Sci* 58:1750–1766
- Kollias P, Jo I, Albrecht BA (2005) High-resolution observations of mammatus in tropical anvils. *Mon Weather Rev* 133:2105–2112
- Labitt M (1981) Coordinated radar and aircraft observations of turbulence. Proj. Rpt. ATC 108. MIT, Lincoln Lab, Cambridge, 40 pp
- Lothon M, Lenschow DH, Leon D, Vali G (2005) Turbulence measurements in marine stratocumulus with airborne Doppler radar. *Q J R Meteorol Soc* 131:2063–2080
- Mechem DB, Kogan YL, Schultz DM (2010a) Large-eddy simulation of post-cold-frontal continental stratocumulus. *J Atmos Sci* 67:3835–3853
- Mechem DB, Kogan YL, Schultz DM (2010b) Large-eddy observation of post-cold-frontal continental stratocumulus. *J Atmos Sci* 67:3368–3383
- Nastrom GD (1997) Doppler radar spectral width broadening due to beamwidth and wind shear. *Ann Geophys* 15:786–796
- Nicholls S (1984) The dynamics of stratocumulus: aircraft observations and comparisons with a mixed layer model. *Q J R Meteorol Soc* 110:783–820
- O'Connor EJ, Illingworth AJ, Brooks IM, Westbrook CD, Hogan RJ, Davies F, Brooks BJ (2010) A method for estimating the turbulent kinetic energy dissipation rate from a vertically pointing Doppler lidar, and independent evaluation from balloon-borne in situ measurements. *J Atmos Oceanic Technol* 27:1652–1664
- Rémillard J, Kollias P, Luke E, Wood R (2012) Marine boundary layer cloud observations at the Azores. *J Clim*. e-View, doi:[10.1175/JCLI-D-11-00610.1](https://doi.org/10.1175/JCLI-D-11-00610.1)
- Rogers RR, Tripp BR (1964) Some radar measurements of turbulence in snow. *J Appl Meteorol* 3:603–610
- Shupe MD, Brooks IM, Canut G (2012) Evaluation of turbulent dissipation rate retrievals from Doppler cloud radar. *Atmos Meas Technol* 5:1375–1385
- Siebert H, Lehmann K, Wendisch M (2006) Observations of small-scale turbulence and energy dissipation rates in the cloudy boundary layer. *J Atmos Sci* 63:1451–1466
- Srivastava RC, Atlas D (1974) Effect of finite radar pulse volume on turbulence measurements. *J Appl Meteorol* 13:472–480
- Stull RB (1988) An introduction to boundary layer meteorology. Kluwer Academic Publishers, Dordrecht, 666 pp
- Wood R (2012) Stratocumulus clouds. *Mon Weather Rev* 140:2373–2423
- Zeman O, Tennekes H (1977) Parameterization of the turbulent energy budget at the top of the daytime atmospheric boundary layer. *J Atmos Sci* 34:111–123
- Zhu P, Albrecht BA, Ghaté VP, Zhu Z (2010) Multiple scale simulations of stratocumulus clouds. *J Geophys Res* 115:D23201. doi:[10.1029/2010JD014400](https://doi.org/10.1029/2010JD014400)